# Reconstruction of x-ray free-electron laser pulse duration and energy chirp from spectral intensity fluctuations

River R. Robles,* Aliaksei Halavanau, David Cesar, Alberto Lutman, and Gennady Stupakov

*SLAC National Accelerator Laboratory, Menlo Park, California 94025, USA*

(Received 16 November 2022; accepted 3 February 2023; published 2 March 2023)

Accurate measurements of the x-ray pulse duration produced by x-ray free-electron lasers (XFELs) typically rely on longitudinal electron beam phase space diagnostics, e.g., an x-band transverse deflecting cavity (XTCAV). An alternative group of methods is based on measurements of radiation statistics and spectral correlations. In this paper, we present a statistical analysis of FEL radiation which extends the previous technique by Lutman *et al.* [Phys. Rev. ST Accel. Beams **15**, 030705 (2012)], including the electron beam energy chirp in the FEL gain model. In doing so, we show that with measurements of the average spectrum and the spectral intensity correlations, one can reconstruct the x-ray pulse length, e-beam chirp, and corresponding spectrometer resolution. We validate our approach with 1D and 3D simulations before moving to an experimental demonstration in which our method finds results similar to those obtained from XTCAV measurements.

DOI: 10.1103/PhysRevAccelBeams.26.030701

## I. INTRODUCTION

X-ray free-electron lasers (XFELs) produce x-ray pulses with a brightness exceeding synchrotron sources by many orders of magnitude [1–5]. The XFEL was revolutionary in particular because of its ability to provide ultrashort, high power x-ray pulses with durations ranging from hundreds of femtoseconds (fs) down to several hundred attoseconds (as). The unique capability of the XFEL to produce short pulses sets it distinctly apart from the storage ring-based light sources.

Measuring the duration of these short pulses is difficult, and many methods have been proposed and demonstrated to do so. Perhaps the most direct method is to measure the electron beam longitudinal phase space using an x-band transverse deflecting cavity (XTCAV), which maps the time and energy coordinates of the electrons onto their transverse positions [6,7]. By evaluating time-dependent energy loss in the bunch after lasing, one can in principle reconstruct the pulse profile, with a resolution of several fs. This is now a common approach at the XFEL facilities that have invested in an XTCAV system. However, some facilities, e.g., European XFEL, do not have an XTCAV system in operation [8]. Furthermore, this method has limited use when the e-beam loss profile does not coincide with the FEL pulse profile, for example, when one bunch lases twice and the XTCAV only measures the final phase space.

Other methods have been proposed which make use of the statistics of FEL radiation to infer information about the pulse duration. A cross-correlation technique proposed in [9] and demonstrated in [10], for example, used a chicane in the middle of the FEL undulator to enable the generation and delay of a second x-ray pulse for cross-correlation with the first, which enabled the evaluation of single pulse duration and dual-pulse separation. This method has some disadvantages, such as the fact that by its nature, it can only measure the pulse duration at the location of the chicane. The cross-correlation method has been recently extended to the case of chirped e-beams in [11]. A related method uses an x-ray split-and-delay line to correlate a given pulse with itself [12,13]. Yet another method measured highly resolved single-shot FEL spectra to determine the spectral width of self-amplified spontaneous emission (SASE) spikes [14]. They estimated the pulse duration by comparing these spike widths to simulations. Their method relied on an assumption of the energy chirp of the electrons driving the FEL process, which they estimated by other means.

A different statistical method was proposed in [15] which resembles similar methods in synchrotron radiation environments [16–19], which inferred the pulse duration from measurements of spectral intensity fluctuations. This method takes advantage of precise theoretical models of the statistics of FEL radiation. Any spectral reconstruction method has the distinct advantage that the only hardware

*riverr@stanford.edu; Also at Department of Applied Physics, Stanford University, Stanford, California 94305, USA.

requirement is an x-ray spectrometer, which is commonly found at XFEL facilities. No additional installation is needed in the electron beamline, unlike the XTCAV and autocorrelation approaches. It was also shown that the spectral intensity correlation approach could predict the pulse length at saturation with a postsaturation taper, which is useful for practical application since most day-to-day FEL operations are in this regime [15]. We would also point out a related method [20] that used multishot spectral measurements to spectrally resolve the time profile of the radiation with an algorithm the authors call ROSA.

Typically, the spectral intensity correlation methods do not account for any energy chirp in the electron beam. The ROSA algorithm is an exception, but while it can reconstruct the temporal profile of the radiation at individual photon energies, it cannot easily provide the full, frequency integrated, temporal profile. By chirp, we mean that the central energy of a given slice varies along the bunch. In the simplest case, this takes a linear form such that the energy of a given electron is tied to its position in the bunch by $\gamma(t) = \gamma_0 + ht$ where $\gamma_0$ is the central energy of the bunch in units of the electron rest mass, $h$ is the chirp parameter in units of rest energy per unit time, though we will often report it equivalently in MeV of energy per micron along the bunch length, and $t$ is the time of arrival of an electron relative to the bunch center. The FEL resonant condition determines the relationship between emitted x-ray frequency and electron energy in the form

$$\omega_r(t) = \frac{2\gamma(t)^2 k_u c}{1 + K^2/2}, \tag{1}$$

where $k_u$ is the undulator wavenumber and $K$ is the undulator strength parameter. A chirp, therefore, broadens the spectral width of the pulse, leading simple frequency correlation methods to underestimate the pulse duration.

Several XFEL operating modes have been proposed which intentionally make use of a chirped beam. These include, for example, short pulse generation by sending a highly chirped pulse through a monochromator [21] or through chirp-taper schemes [22]. Also of interest would be to implement chirped pulse amplification at an x-ray free-electron laser [23,24], which would enable TW level peak powers. Many fresh slice methods also take advantage of a chirped beam to ensure only a small slice of the beam lases [25]. For all of these methods, and any others which would rely on a chirped beam, it is essential to understand the value of the chirp.

In this article, we formally extend the spectral correlation approach to linearly chirped electron beams by using the 1D FEL Green's function with a linear chirp. We find that we can reconstruct not only the pulse duration but also the value of the electron beam chirp and the resolution of the spectrometer measurement. We benchmark our method using 1D and 3D FEL simulations and show that it retains its accuracy into early saturation. We then compare the method against experimental XTCAV measurements, finding similar results.

We stress that our model is not parameter free: it requires a model guess of the shape of the temporal profile of the x-ray pulse as well as an estimate of the bandwidth of the SASE FEL process. We discuss the limitations of these free parameters in the text, finding that for the cases of most interest, these quantities are known with enough precision at experimental facilities. Furthermore, any method attempting to extract average parameters of the FEL will be sensitive to machine jitter. Extracting the average energy chirp and pulse length makes sense only if electron bunch energy and length jitter is accounted for. This can be done by filtering on other beamline diagnostics, as we show in Sec. IV.

## II. THEORETICAL APPROACH

The premise of the approach is to calculate the spectral intensity correlation function $G_2(\omega, \delta\omega)$, defined below, within some appropriate theoretical model, which can then be used to fit measured spectra to extract the relevant parameters. We largely follow the approach laid out in [15] calculating the intensity correlation function $G_2(\omega, \delta\omega)$ with appropriate modifications for the chirp. For clarity, we list key variables and their meaning in Table I in the order they appear in this section.

The measurement is a convolution of the true intensity spectrum with a spectrometer instrument function which we assume to be Gaussian:

$$\tilde{S}(\omega) \equiv \int \frac{d\omega_0}{2\pi} e^{-\frac{(\omega-\omega_0)^2}{2\sigma_m^2}} |\tilde{E}(\omega_0)|^2, \tag{2}$$

TABLE I. Key variables used throughout the paper.

| Variable | Meaning |
|---|---|
| $E(t)$ | Time-domain SASE electric field |
| $\tilde{E}(\omega)$ | Frequency domain SASE field |
| $\tilde{S}(\omega)$ | Measured spectral intensity |
| $\sigma_m$ | rms spectrometer energy resolution |
| $G_2(\omega, \delta\omega)$ | Measured spectral intensity correlation function |
| $h$ | e-beam energy chirp |
| $u$ | e-beam chirp in terms of resonant energy shift |
| $\gamma_0$ | Average e-beam Lorentz factor |
| $\omega_0$ | Resonant photon frequency |
| $g(t)$ | Time-independent FEL Green's function |
| $\rho$ | FEL Pierce parameter |
| $\sigma_\omega$ | Bandwidth of unchirped SASE |
| $h_{\mathrm{td}}(t_j)$ | Time-dependent part of FEL Green's function |
| $\chi(t)$ | Average x-ray temporal profile $\propto \langle E(t)^2 \rangle$ |
| $\tilde{g}(\omega)$ | Fourier transform of $g(t)$ |
| $\sigma_t$ | rms duration of the x-ray pulse |
| $\tilde{W}(\omega)$ | Weighting function for $G_2(\omega, \delta\omega)$ |
| $G_2(\delta\omega)$ | Average of $G_2(\omega, \delta\omega)$ weighted by $\tilde{W}(\omega)$ |

where $\sigma_m$ is the spectrometer resolution and $\tilde{E}(\omega)$ is the SASE electric field in the frequency domain. We define the measured spectral intensity correlation as

$$G_2(\omega,\delta\omega) \equiv \frac{\langle \tilde{S}(\omega-\frac{\delta\omega}{2})\tilde{S}(\omega+\frac{\delta\omega}{2})\rangle}{\langle \tilde{S}(\omega-\frac{\delta\omega}{2})\rangle\langle \tilde{S}(\omega+\frac{\delta\omega}{2})\rangle} - 1 \tag{3}$$

where $\langle . \rangle$ indicates an ensemble average over many statistically independent shots of the FEL. The time-domain electric field $E(t)$ produced by a SASE free-electron laser driven by a linearly chirped, infinitely long electron beam was studied by Krinsky and Huang in [26]. We have re-derived their result in Appendix A to explicitly account for a finite electron bunch. We write the result in the following form for easy comparison with [15]:

$$E(t) = \sum_{j=1}^{N_e} e^{i\omega_j(\frac{z}{c}-(t-t_j))} g(t-t_j) h_{\mathrm{td}}(t_j), \tag{4}$$

where $\omega_j = \omega_0 + u t_j$ is the frequency of light emitted by the $j$th electron which is the central frequency $\omega_0$ offset by a term proportional to the chirp $u$, $g(t)$ is the time-independent FEL Green's function, and $h_{\mathrm{td}}(t)$ is a time-dependent factor attached to the Green's function. The latter two will be explained in more detail below. We note that the chirp $u = \dot{\omega}_r$, where a dot indicates a time derivative, is related to the electron beam chirp $h = \dot{\gamma}$ by the resonance condition [Eq. (1)]: $u = 2\omega_r h/\gamma_0$. The time-independent Green's function for the FEL interaction is [26]

$$g(t) \propto \exp\left[-b\left(t-\frac{z}{v_g}\right)^2 - \frac{iu}{2}\left(t-\frac{z}{v_0}\right)\left(t-\frac{z}{c}\right)\right] \tag{5}$$

where $b = \frac{3}{4}(1+\frac{i}{\sqrt{3}})\sigma_\omega^2$ and $\sigma_\omega^2 = \frac{3\sqrt{3}\rho}{k_u z}\omega_0^2$ is the square of the inherent bandwidth of SASE. Furthermore, $v_g = \omega_0/(k_r + \frac{2}{3}k_u)$ and $v_0 = \omega_0/(k_r + k_u)$ with $k_r = 2\pi/\lambda_r$, the radiation wavenumber, $k_u = 2\pi/\lambda_u$, the undulator wavenumber, and $\omega_0$, the central resonant FEL frequency.

The Green's function $g(t)$ is called time-independent because its contribution to the field depends only on the relative time $t - t_j$. The function $h_{\mathrm{td}}(t_j)$ is a stand-in for any time-dependent effects in the gain process which are slow compared to the FEL coherence length, such as variations in the e-beam current profile and gain reduction due to the chirp. Although its particular dependence on these various effects can in principle be derived analytically, as we did for chirp and current effects in Appendix A, we show in Appendix B that it can more generally be related to the average temporal x-ray intensity profile of the FEL $\chi(t) = \langle |E(t)|^2 \rangle$. With these definitions, the frequency domain field is defined by the Fourier transform

$$\tilde{E}(\omega) \equiv \int e^{i\omega t} E(t) dt = \sum_j e^{i(\frac{\omega_j}{c}z + \omega t_j)} \tilde{g}(\omega-\omega_j) h_{\mathrm{td}}(t_j) \tag{6}$$

where $\tilde{g}(\omega) \equiv \int e^{i\omega t} g(t) dt$. The explicit calculation of the various terms relevant to $G_2$ is relegated to Appendixes B and C. Unlike the chirpless case, it is difficult to write a succinct general expression for $G_2$ for an arbitrary pulse profile. For a Gaussian x-ray intensity profile, $\chi(t) = e^{-t^2/2\sigma_t^2}$, we find $G_2$ in the form

$$G_2(\omega,\delta\omega) = \frac{1}{\sqrt{1+2\sigma^2\sigma_t^2}} \exp\left[-\frac{\delta\omega^2\sigma_t^2\xi_0^2}{1+2\sigma^2\sigma_t^2}\right] \tag{7}$$

where to make an explicit connection to [15], we define

$$\sigma = \frac{\sqrt{2}\sigma_m\sigma_\omega}{\sqrt{\sigma_m^2 + (1+\delta_u^2)\sigma_\omega^2}} \qquad \xi_0 = \frac{\sigma_\omega^2\sqrt{1+\delta_u^2}}{\sigma_m^2 + (1+\delta_u^2)\sigma_\omega^2} \tag{8}$$

where $\delta_u^2 = \tilde{u} + \tilde{u}^2(1+3\sigma_t^2\sigma_\omega^2)$ with $\tilde{u} \equiv u/\sqrt{3}\sigma_\omega^2$. If the bunch is long enough that $\frac{u\sigma_t}{\sigma_\omega}$ is of order 1, then $\delta_u \simeq u\sigma_t/\sigma_\omega$. We note that taking $\delta_u = u\sigma_t/\sigma_\omega$ in this way is equivalent to neglecting the modification to the time-independent Green's function from the chirp in Eq. (5). In addition, taking the limit $u \to 0$ reduces Eq. (7) to Lutman's original expression [15]. We note that in the theory, $G_2$ no longer depends on the central frequency $\omega$, only on the frequency shift $\delta\omega$. Finally, we also note that the average measured spectral intensity can be written as

$$\langle \tilde{S}(\omega) \rangle \propto \exp\left[-\frac{(\omega-\omega_0)^2}{2[\sigma_m^2 + \sigma_\omega^2(1+\delta_u^2)]}\right] \tag{9}$$

For an arbitrary pulse profile $\chi(t)$, these functions can be calculated numerically in accordance with the equations of Appendix C.

We will now outline the procedure by which knowledge of an analytic form for the $G_2$ function and the average spectrum $\langle \tilde{S}(\omega) \rangle$ can be used to reconstruct the pulse length, chirp, and spectrometer resolution given a set of spectral measurements. We will refer specifically to Eqs. (7) and (9), but the same logic can be applied to any numerically derived forms for $G_2$ and $\langle \tilde{S} \rangle$ for an arbitrary pulse profile $\chi(t)$. For a given set of spectra, Eq. (3) can be used to calculate the spectral intensity correlation, and $\langle \tilde{S}(\omega) \rangle$ is simply the average of the measurement data. One can then fit Eqs. (7) and (9) to these experimental functions, respectively, and from there can extract the amplitude and width of $G_2$ as well as the width of the spectrum. Solving for the unknown variables yields $\sigma_m$, $u$, and $\sigma_t$ as functions of the SASE bandwidth $\sigma_\omega$. In practice, we will often report $h$ in place of $u$. The SASE bandwidth $\sigma_\omega$ can be calculated as before as $\sigma_\omega^2 = \frac{3\sqrt{3}\rho}{k_u z}\omega_0^2$ in the 1D limit or using an appropriate model of the SASE bandwidth in the 3D regime. This can be done by a number of methods, such as gain length measurements, FEL simulations, estimation by the Ming Xie fitting

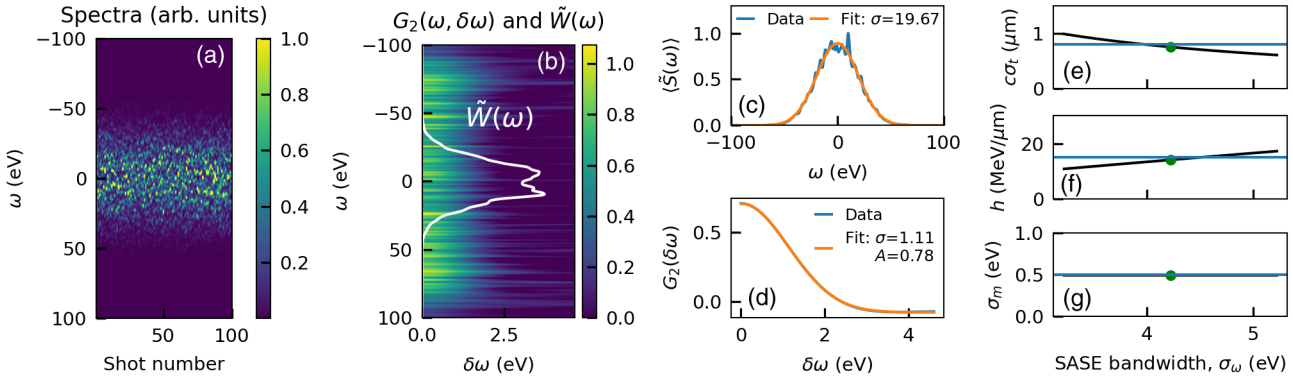


FIG. 1. The steps of the reconstruction method are outlined. (a) shows a set of simulated spectra. These are used to calculate $G_2(\omega,\delta\omega)$ [Eq. (3)] and the weight function [Eq. (10)] $W(\omega)$ (b). The titles of (a) and (b) act as labels for their color bars. Averaging $G_2(\omega,\delta\omega)$ weighted by $W(\omega)$ yields $G_2(\delta\omega)$ [Eq. (11)] (d) and an average of the spectra yields $\langle\tilde{S}(\omega)\rangle$ (c). Fitting Gaussian functions to each of them allows us to extract widths and amplitudes that can be used to solve for $\sigma_t$ (e), $h$ (f), and $\sigma_m$ (g) as functions of $\sigma_\omega$ [Eqs. (7) and (9)]. The black lines indicate these reconstructed values. The blue horizontal lines indicate the true values of each parameter, whereas the green dot indicates the predicted value at the guessed SASE bandwidth.

formulas [27], or by solving the FEL dispersion relations as a function of frequency detuning [28]. The SASE bandwidth formula given above only applies during exponential gain: at saturation, the bandwidth saturates at the approximate value $\rho\omega_0$. To apply the method to the saturation regime, the accuracy of the model can be maintained if $\sigma_\omega(z)$ is calculated as $\sigma_\omega(z) = \max\left(\sqrt{\frac{3\sqrt{3}\rho}{k_u z}}\omega_0, \rho\omega_0\right)$. We will take this convention into the results of this paper.

This approach requires one caveat, which is that although in the theory, the calculated form of $G_2(\omega,\delta\omega)$ does not actually depend on $\omega$, our model only accurately predicts statistics near the center of the FEL resonance where the spectrum is dominated by the high-gain FEL process. The edges of the spectrum contain non-negligible contributions from other processes and thus $G_2$ can be different. Thus, in practice, the measured $G_2(\omega,\delta\omega)$ should be averaged over $\omega$ with a suitable weight function that selects for frequencies around which we collect appropriate statistics. Such a function was proposed by Lutman in [15],

$$\tilde{W}(\omega) = \frac{\int db\langle\tilde{S}(\omega-\frac{b}{2})\rangle\langle\tilde{S}(\omega+\frac{b}{2})\rangle}{\int dbd\omega\langle\tilde{S}(\omega-\frac{b}{2})\rangle\langle\tilde{S}(\omega+\frac{b}{2})\rangle} \tag{10}$$

The particular form of this function ensures that we are only gathering statistics from portions of the spectrum with large signal. Thus, the measure of $G_2$ used in practice should actually be

$$G_2(\delta\omega) = \int d\omega\tilde{W}(\omega)G_2(\omega,\delta\omega). \tag{11}$$

Note that because of the normalization of $\tilde{W}$, this does not change our theoretical results.

Figure 1 illustrates the approach we have outlined using the sample set of 100 simulated spectra depicted in Fig. 1(a). With these spectra, we are able to calculate $G_2(\omega,\delta\omega)$ as well as the weight function $\tilde{W}(\omega)$ using Eqs. (3) and (10), respectively. Averaging $G_2(\omega,\delta\omega)$ weighted by $\tilde{W}(\omega)$ as in Eq. (11) yields $G_2(\delta\omega)$ shown in Fig. 1(d), and averaging the original spectra yields the average spectrum $\langle\tilde{S}(\omega)\rangle$ in Fig. 1(c). These are both fit to Gaussian, which enables us to calculate $\sigma_t$, $h$, and $\sigma_m$ all as functions of the SASE bandwidth using Eqs. (7) and (9). These curves are shown as black lines in Fig. 1(e)–(g). The green dot in those plots shows the values at the predicted value of the SASE bandwidth for that simulation, showing excellent agreement with the blue horizontal lines which indicate the true values of each parameter. Several features of these plots are indicative of more general features of our model, for example, that the reconstructed spectrometer resolution is independent of the SASE bandwidth, and that when the spectral bandwidth is much broader than the SASE bandwidth, the reconstructions of $h$ and $\sigma_t$ are quite insensitive to the SASE bandwidth.

As demonstrated in [29] and later in this article, the sensitivity to the SASE bandwidth is highest when $u\sigma_t < \sigma_\omega$, in which case the chirp is unimportant for the properties of the x-ray pulse and thus should not impact user experiments. When the chirp is important, i.e., when $u\sigma_t > \sigma_\omega$, the measurement is quite insensitive to the SASE bandwidth. A more fundamental uncertainty in our model is that the calculated values of $G_2$ and the average spectrum do not depend strongly on the sign of the chirp $u$, so in general, our method cannot extract the sign of the chirp, only the absolute value. The sign of the chirp can be determined in practice by scanning some machine parameter that talks to chirp such as accelerating phase.

Another uncertainty in our approach is the need to provide a guess of the x-ray pulse shape, $\chi(t)$, which was also required of the zero chirp approach of [15]. Of course, one can always use the Gaussian model to get

approximate results which may be sufficient for many purposes. A more precise answer comes from Appendix C, where we showed in Eq. (C4) that, for a large chirp, the spectrum starts to resemble the x-ray pulse temporal profile. Thus, for example, a flattopped measured spectrum implies a flattopped x-ray pulse while a Gaussian measured spectrum implies a Gaussian pulse. For weaker chirps, the message is not as clear, as the spectrum, in that case, is generally a convolution of the Gaussian SASE spectrum with the pulse profile, and for zero chirp, one cannot infer the pulse profile from the spectrum. For our cases of interest, where we anticipate there being a chirp, the measured spectrum provides insight into the appropriate choice of x-ray pulse shape $\chi(t)$.

## III. FEL SIMULATIONS

We now proceed to demonstrate the validity of our model with a series of simulations. First, we use a 1D FEL code to benchmark our approach in a regime matching the theory in order to understand the model's capabilities and limitations. Afterward, we move on to the 3D code GENESIS [30], which will allow us to test the model in the presence of more realistic 3D effects which are not explicitly captured by the 1D Green's function.

To mimic an experimental measurement with nonideal spectrometer effects, we numerically convolve the simulated spectra with a Gaussian instrument function as in Eq. (2). When this is done in the data to follow, we will report the imposed resolution $\sigma_m$ explicitly.

Finally, in what follows all of our reconstructions of the pulse length and chirp will be plotted with error bars to indicate the sensitivity of the method to the calculated SASE bandwidth. Specifically, the central dot will indicate the value at the theoretical SASE bandwidth, and the error bars will indicate the values at $\pm 0.5$ eV from that theoretical value. We choose 0.5 eV because few eV SASE bandwidths are typical across a large photon energy range, and even this $> 10\%$ uncertainty will be seen to have a small impact on our reconstructions.

### A. 1D FEL simulations

For the 1D simulation studies, we have generated two sets of data: one with a fixed bunch length and variable chirp and another with a fixed chirp and variable bunch length. For each data point (i.e., each set of chirp and bunch length), we performed 1000 statistically independent simulations. The parameters shared by all of the 1D simulations are reported in Table II, with the caveat that the quoted rms bunch length and chirp values are for the fixed length and fixed chirp datasets, respectively.

In our first demonstration of the model, we fixed the electron bunch rms length at 2 μm and scanned the imposed chirp. For this initial study, we neglected any spectrometer resolution ($\sigma_m = 0$). The results of this study

TABLE II. 1D FEL simulation parameters.

| Parameter | Unit | Value |
|---|---|---|
| Beam energy | GeV | 12.1 |
| Beam energy spread | MeV | 0.726 |
| Normalized emittance | μm rad | 0.6 |
| Peak current | kA | 3 |
| $\beta$ function | m | 25 |
| Undulator period | cm | 3 |
| Undulator $K$ | | 3.5 |
| Radiation wavelength | nm | 0.19061 |
| Bunch shape | | Gaussian |
| rms bunch length | μm | 2 |
| Chirp | MeV/μm | 7.5 |
| Undulator length | m | 30 |

are shown in Figure 2, with Figure 2(a) showing the x-ray pulse length and Figure 2(b) showing the e-beam chirp. The data points are as found from the simulation (blue), from the no chirp $G_2$ formula of [15] (green), and from the current revised method (orange). Figure 2(a) clearly demonstrates the need to account for e-beam chirp in the spectral reconstruction method. As the chirp increases, the bunch length predicted by the original method steadily drops, whereas the current method is accurate across the entire range of simulated chirps.

This effect can be understood by taking the large chirp limit of equation (7), which for $\sigma_m = 0$ is $G_2(\omega, \delta\omega) \simeq \exp[-\delta\omega^2\sigma_\omega^2/u^2]$. In the original formalism of [15], the measured $G_2$ is interpreted as $\exp[-\delta\omega^2\sigma_t^2]$, thus in the limit of large chirps, the original method inadvertently sets $\sigma_t = \sigma_\omega/|u|$. This explains the steadily decreasing prediction from the original method in Figure 2(a) as the chirp $u$ is increased. In the same vein, Figure 2 serves to clarify the regime in which our model is the most accurate with respect to chirp prediction: the chirp can only be predicted with a high level of accuracy if it has a quantifiable impact on the spectra. If $u\sigma_t \ll \sigma_\omega$, then the uncertainty in the SASE

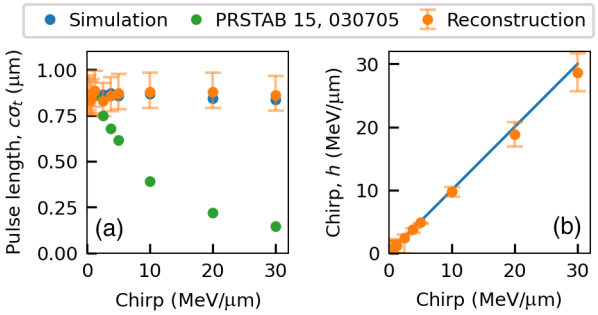


FIG. 2. Results for a scan of the e-beam chirp in 1D simulations. The left and right show the x-ray pulse length and e-beam chirp, respectively, as obtained from the simulation (blue), from our reconstruction model (orange), and from the model of [15] (green).

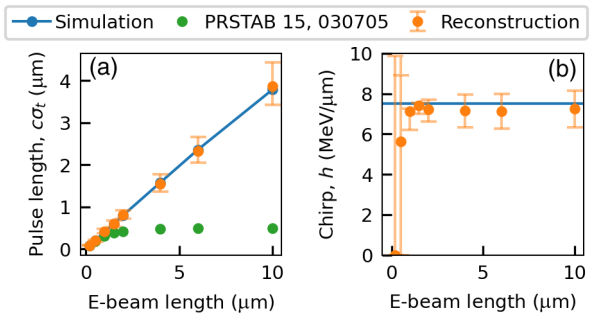


FIG. 3. Results for a scan of the e-beam length in 1D simulations. The left and right show the x-ray pulse length and e-beam chirp, respectively, as obtained from the simulation (blue), from our reconstruction model (orange), and from the model of [15] (green).

bandwidth prevents one from measuring that small chirp with high accuracy.

In Fig. 3, we report the results of the reconstruction for a fixed 7.5-MeV/μm chirp and bunch length variable between 0.2 and 10 μm. We have again neglected spectrometer resolution for now. Figure 3(a) shows the x-ray pulse length as a function of the electron bunch length with the same color scheme as Fig. 2. As discussed above, in the limit of large chirp, the pulse length dependence drops out of $G_2(\delta\omega)$, which leads to the zero chirp prediction of [15] to asymptotically approach $\sigma_\omega/|u|$. In the short pulse regime where the impact of the chirp on the spectrum is weak, similarly, our reconstruction converges on both the simulated values and the zero chirp reconstruction. We also note that our model reconstructs the shortening of the x-ray pulse relative to the e-beam length which derives from the time-dependence of the gain length in the varying Gaussian current profile. These same arguments explain the chirp reconstruction shown in Fig. 3(b). For $u\sigma_t < \sigma\omega$, the impact on the spectrum is weak and thus our spectral reconstruction is not very accurate. For longer pulses, on the other hand, the pulse is extracted with high accuracy.

Let's now turn our attention to the effect of finite spectrometer resolution. There is a limit to how high the resolution can be before the reconstruction breaks down. Naively, one expects this when the spectrometer can no longer resolve individual SASE spikes. The spectral width of a SASE spike is described by the spectral coherence defined as [26]

$$\sigma_{\mathrm{coh}} = \int d\omega_1 \left| \frac{\langle \tilde{E}(\omega - \omega_1/2)\tilde{E}^*(\omega + \omega_1/2)\rangle}{\langle |\tilde{E}(\omega)|^2 \rangle} \right|^2 \qquad (12)$$

This is easily computed with our theoretical model, and for a Gaussian pulse in the limit $\sigma_t\sigma_\omega \gg 1$ and to the lowest order in the chirp, we find

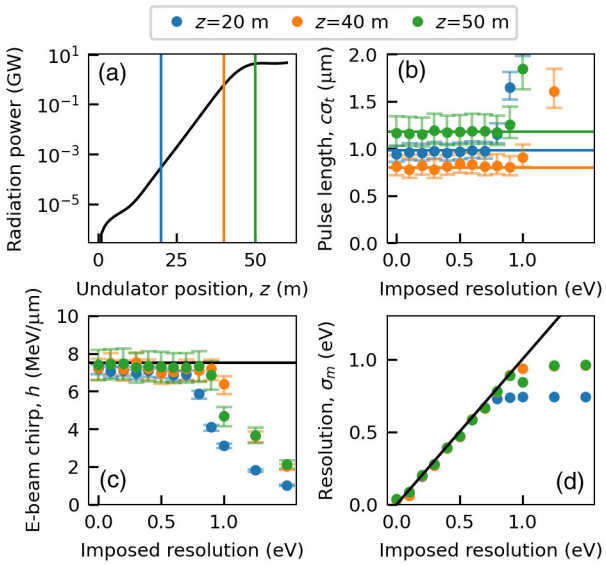


FIG. 4. Results from 1D simulations scanning the spectrometer resolution for a fixed 7.5-MeV/μm e-beam chirp. (a) shows the average radiation power along the undulator marking $z = 20$ m (blue), $z = 40$ m (orange), and $z = 50$ m (green). (b), (c), and (d) show the reconstructed pulse length, e-beam chirp, and spectrometer resolution as a function of imposed spectrometer resolution at those three locations.

$$\sigma_{\mathrm{coh}} = \sqrt{\pi}\sqrt{\frac{1}{\sigma_t^2} + \frac{u^2}{\sigma_\omega^2}} \qquad (13)$$

Taking the case study of Fig. 3 at the 2-μm bunch length working point, we find that at $z = 30$ m, for example, $\sigma_{\mathrm{coh}} = 0.65$ eV. The terms from the pulse length and the chirp contribute 0.13 and 0.47 eV, respectively, in quadrature.

We study the interplay of the spectrometer resolution with the reconstruction procedure in Fig. 4, which presents a variety of results related to 2-μm pulse length, 7.5-MeV/μm chirp simulations with varying spectrometer resolutions. Figure 4(a) reports the output power of the FEL as a function of distance into the undulator in order to denote different locations in $z$ according to their relation to the stages of the FEL gain process. In particular, lines are drawn at $z = 20$ m, $z = 40$ m, and $z = 50$ m denoting early exponential gain, late exponential gain, and early saturation. The color of these lines corresponds with the colors of the dots in the subsequent plots.

The calculated spectral coherence at these three points is 0.54, 0.75, and 0.77 eV, respectively. We expect that our approach will retain its accuracy up to around these thresholds. Indeed, this is born out in Figs. 4(b)–4(d), which show the pulse length, chirp, and spectrometer resolution as predicted by our model as we scan the imposed spectrometer resolution to higher values. The solid lines in each plot indicate the true value for the given color, with black lines indicating true values that do not

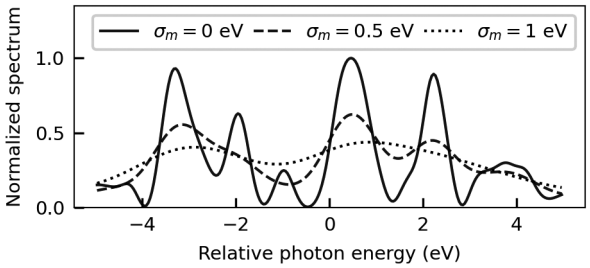


FIG. 5. A typical single-shot spectrum from 1D simulations at $z = 40$ m showing the impact of 0-, 0.5-, and 1.0-eV measurement resolution.

depend on $z$. The blue data points in each plot start to diverge from the true values around $\sigma_m = 0.75$ eV, while the orange points deviate around $\sigma_m = 1$ eV. Up to those points, each of the reconstructions is highly accurate when the SASE bandwidth is known with $\pm 0.5$ eV precision. The saturation data points follow similar behavior to the late exponential gain regime points, which is consistent with the fact that the spectral coherence at $z = 40$ m is very nearly the saturated value.

The effect of these degrees of resolution on the measured spectra can be better understood with the help of Fig. 5, in which we plot a typical single shot spectrum at $z = 40$ m in a $\pm 5$ eV window for 0-, 0.5-, and 1-eV measurement resolution. Already, 0.5-eV resolution limits our ability to resolve weaker spikes by eye, and with 1-eV resolution, only the approximate locations of the strong peaks can be guessed. Nevertheless, our model was able to extract pulse length, chirp, and resolution even at $\sigma_m = 0.5$ eV and only begins to break down at 1 eV in late exponential gain and early saturation. Finally, we note that the required relative spectral resolution is typically achievable in soft x-ray (SXR) or hard x-ray (HXR) spectrometers [15,31,32].

### B. 3D FEL simulations

With the model's validity now established in the 1D regime, we move to 3D simulations using the code GENESIS 1.3 v4 [30,33]. The parameters relevant to the 3D simulations are given in Table III. They differ slightly from the 1D simulations but still focus on an LCLS-like hard x-ray configuration using the LCLS-II undulators. The simulations are performed using the standard LCLS-II magnetic lattice, and therefore include gaps between undulator modules, and no undulator tapering.

The 3D aspect of the simulations introduces several potentially complicating factors, such as transverse coherence effects and the 3D modification of the SASE gain and bandwidth. Although the FEL is known to produce almost fully transversely coherent pulses, it is not perfect. Lutman *et al.* measured the number of spectral modes in an XFEL pulse while changing the integrated transverse cross section of the pulse in the spectrometer [34]. They found that for moderate cross sections, the mode number is independent

TABLE III. 3D FEL simulation parameters.

| Parameter | Unit | Value |
|---|---|---|
| Beam energy | GeV | 10.023 |
| Beam energy spread | MeV | 2.03 |
| Normalized emittance | μm rad | 0.4 |
| Peak current | kA | 3 |
| $\beta$ function | m | 12.12 |
| Undulator period | cm | 2.6 |
| Undulator $K$ | | 2.407 |
| Radiation wavelength | nm | 0.13789 |
| Bunch shape | | Gaussian |
| rms bunch length | μm | 2 |

of the cross-section size, but at a certain threshold, it starts to increase. This threshold effect is indicative of incomplete transverse coherence. On the other hand, the weak dependence on cross section prior to that threshold indicates that as long as the transversely coherent fraction of the pulse is considered, the statistics are fundamentally unchanged from the 1D FEL. The key change is the modification of the SASE bandwidth due to 3D gain degrading effects. Since our model relies on a guess of the SASE bandwidth, it is particularly important to take this change into account. In our case, we used zero chirp GENESIS simulation results to estimate the uncorrelated SASE bandwidth. We found that it corresponded to the 1D formula given we used $\rho_{\text{eff}} = 4.49 \times 10^{-4}$. For reference, the true 1D Pierce parameter is $\rho = 7.34 \times 10^{-4}$.

To emulate an experimental measurement, we propagate the simulated fields to the far field, using Fresnel propagation to 100 m downstream of the source point which is roughly in line with the distance from the LCLS undulators to the LCLS HXR spectrometer [32]. The spectrum is then "measured" in a $\pm 30$ μm window, emulating experimental slits. This particular slit size is chosen to align with the region of transverse coherence in the beam, as will be shown in Fig. 6. We have found the difference between the results obtained from this procedure and from simply taking the on-axis far field spectrum to be negligible, which again confirms the observations of [34] that the SASE statistics are essentially 1D within the transversely coherent fraction of the beam.

We performed 3D simulations for chirp values of 0, 15, and 30 MeV/μm. We ran 100 statistically independent simulations at each chirp and confirmed that this number was sufficient to converge on the predictions reported below. The results of the reconstruction model are summarized in Fig. 6. Figure 6(a) plots the radiation power as a function of the undulator position for the three chirp values, Fig. 6(b) shows the pulse length reconstruction, and Fig. 6(c) shows the chirp reconstruction. In the latter two, a solid line indicates a simulation result and dots indicate reconstructed results. Also in Fig. 6(a), we show the average transverse intensity profile (propagated to the far

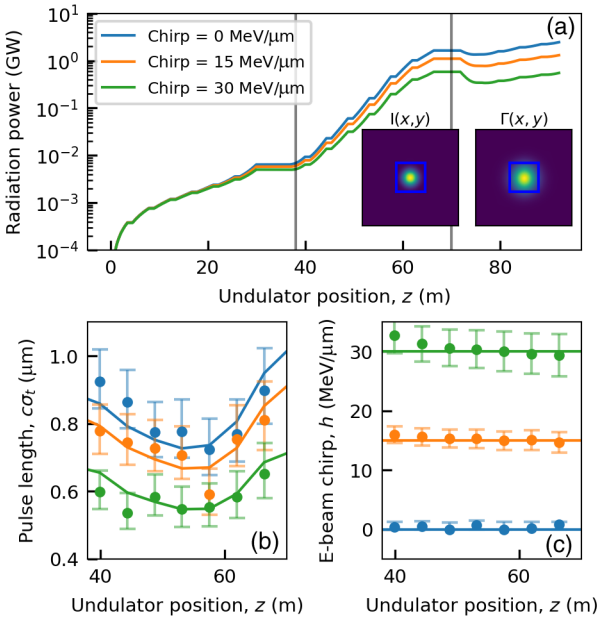


FIG. 6. Results from 3D simulations for three different values of the e-beam chirp. (a) shows the average radiation power for 0, 15, and 30 MeV/μm chirp. (b) and (c) show the reconstructed pulse length and chirp (dots) alongside the true values obtained from the simulations (lines) in the exponential gain and early saturation regimes. (a) also shows the average far field transverse intensity profile as well as the transverse intensity correlation function $\Gamma(x,y)$ at $z = 57.5$ m. The image axes run between $\pm 100$ μm in both directions.

field) $I(x,y) = \langle |E(x,y|)^2 \rangle$ for the central frequency, as well as the transverse intensity correlation function $\Gamma(x,y) = \int dx'dy' \langle I(x',y')I(x+x',y+y') \rangle$ for $z = 57.5$ m. The blue bounding box in these figures indicates the slitted region over which the spectrum is averaged. The fact that the transverse intensity correlation function is well captured by this box indicates that we are measuring the transversely coherent fraction of the beam.

Of immediate interest is the fact that for the 3D simulations, the chirps we have chosen are large enough to impact the growth of the FEL power. Nevertheless, we observe excellent agreement between the simulated and reconstructed values of the pulse length and electron beam chirp. We are even able to account for the slight pulse compression effects observed in Fig. 6(b), in which pulse length drops with an increasing chirp. This phenomenon can be explained with Eq. (A17), which includes a gain degradation factor proportional to the square of the chirp and inversely proportional to the cube root of the e-beam current profile. On the edges of the electron beam, this gain degradation term is enhanced, thereby leading to effective pulse shortening. It is stronger for larger chirps due to the scaling with the square of the chirp. Even without knowing these details explicitly, they are implicitly carried by $h_{\mathrm{td}}$ which as we have already discussed is directly related to the x-ray pulse profile $\chi(t)$.

## IV. EXPERIMENTAL DEMONSTRATION

Finally, we report experimental results demonstrating the utility of our method in user experiments. The measurements were taken at the LCLS in 2016 as part of an x-ray absorption spectroscopy experiment with high-bandwidth XFEL pulses [35]. 12.55-GeV electrons were used to lase at 7.1 keV. To enlarge the bandwidth of the FEL beyond that enabled by normal SASE operation, the beam was intentionally overcompressed leading to a large chirp. The LCLS x-band transverse deflecting cavity (XTCAV) was used to image the e-beam longitudinal phase space after lasing. The x-ray spectra were simultaneously measured with the x-ray pump probe (XPP) instrument. The spectrometer, described in [35], employed a 10-μm thick (220) Si membrane analyzer and had an expected resolution of 0.5 eV at 7.1-keV photon energy. To validate our method, we compared the pulse length and chirp values resulting from our method and the ones obtained from XTCAV images. This provides a useful test of our model also because the experiment went into the saturation regime with a post-saturation taper. This regime is hard to study analytically but is extremely relevant for day-to-day FEL operations. The zero-chirp spectral reconstruction approach of [15] was found to still work in this case, which provides some confidence that our approach should work as well.

Several values of the chirp were tested during the experiment. In Fig. 7, we show two characteristic XTCAV images from two different overcompression working points. Both display energy loss near $t = 0$ indicative of the region of most dominant FEL lasing. This region overlaps, in both cases, with a region of predominantly linear chirp in the electron beam. Figures 7(a) and 7(b)

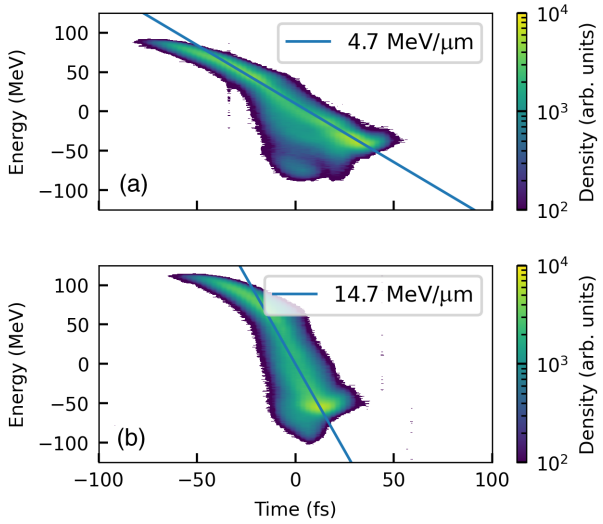


FIG. 7. Representative XTCAV images are shown for 4.7 (a) and 14.7 (b) MeV/μm chirps. In each case, the beam has undergone lasing that is evident from the energy loss around 0 fs. Blue lines give estimates of the linear chirp in the lasing regions.

correspond to linear chirps of 4.5 and 14.7 MeV/μm, as shown in the figure with blue eye-guiding linear fits. We can estimate the approximate duration of the x-ray pulses by fitting them to the regions of energy loss. Furthermore, we introduce uncertainties in the measured values by taking into account the ≈2–3 fs time resolution of the TCAV at this photon energy [6,7]. For the higher chirp case, the energy loss region is less pronounced, leading to a higher uncertainty deriving from the fitting procedure. We find rms durations of $9 \pm 2$ fs ($6 \pm 3$ fs) for the $4.7 \pm 0.2$ MeV/μm ($14.7 \pm 1.2$ MeV/μm) case.

We will now describe how we used the available spectra and other LCLS diagnostics to apply our reconstruction method. This starts by selecting appropriate shots with which to measure statistics. As mentioned in the introduction, measuring the average pulse length and chirp is reasonable only if we filter shots to circumvent energy and bunch length jitter. The LCLS is equipped with a diagnostic that estimates the peak current of the bunch after the last bunch compressor by measuring the coherent edge radiation emitted from the last bend of the compressor, with a typical accuracy at the 5% level [36,37]. With this, we were able to filter to a ±50 A window around 2 kA (3.9 kA) for the 4.5 (14.7) MeV/μm chirp cases. Additionally, the LCLS uses beam position monitors located in dispersive sections of the accelerator to measure the beam energy at the end of the linac with $10^{-4}$ level accuracy [37]. With this, we could further filter our shots to have energies within 1 MeV of 12.55 GeV. This left us with about 200 shots at each working point after filtering.

With these filters defined, we are able to estimate the SASE bandwidth. We use Ming Xie's fitting formula to estimate the effective Pierce parameter of the FEL [27]. The photon energy, beam energy, and current have been previously specified. The undulator period is $\lambda_u = 3$ cm. In addition to these, we assume standard LCLS hard x-ray figures of merit for the other necessary parameters: a 0.4-μm normalized emittance, 10-m $\beta$ function, and 2-MeV slice energy spread at 2-kA peak current. Based on these values, we can estimate an SASE bandwidth $\sigma_\omega \simeq \rho_{\mathrm{eff}}\omega$ of 4.1 eV (5.0 eV) for the 4.7(14.7)-MeV/μm chirp case.

We now have all of the information needed to apply our method. We show the results of our reconstruction in Fig. 8. Figures 8(a) and 8(b) show the average spectrum and the measured $G_2$ with Gaussian fits to each for both cases. As expected, the larger chirped beam has a broader spectrum and broader $G_2$ function. In addition to these expected features, we observed weaker second peaks 20 and 40 eV away from the main spectral peaks. These could result from a number of effects, for example, the fact that our phase spaces are not perfectly linear.

With these fits, we can extract the pulse length and chirp as a function of SASE bandwidth in Figs. 8(c) and 8(d), respectively, which we have done using a Gaussian assumption for the x-ray pulse profile. Based on our prior discussion, we decided that a Gaussian profile made sense

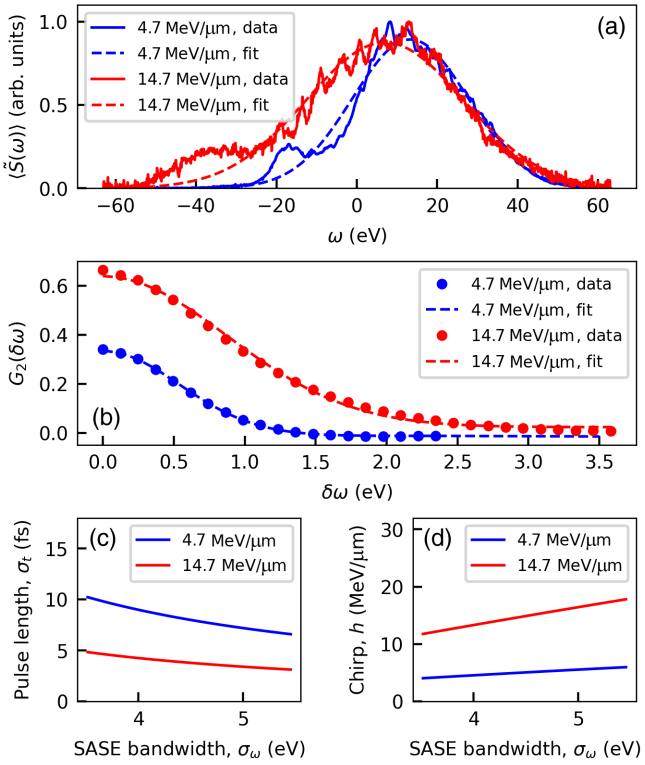


FIG. 8. The average spectra (a) and spectral intensity correlation functions (b) are plotted for the two chirp configurations described in the text, including Gaussian fits to each. From these, we extract pulse length (c) and chirp (d) for the two cases as a function of the SASE bandwidth.

given the Gaussian shape of the spectra. Table IV reports the results for the smaller chirp case with the SASE bandwidth taken to be $4.1 \pm 0.5$ eV. The 4.1-eV central value was discussed above, while the 0.5-eV uncertainty accounts for possible errors in slice energy spread, which is difficult to evaluate for short chirped bunches, and peak current. We observe excellent agreement between the XTCAV measurements and our reconstruction. The extracted resolution, which in theory does not depend on the SASE bandwidth and therefore is reported without an error estimate, is similar to the expected 0.5-eV resolution of the spectrometer.

Table V reports the same results for the larger chirp working point. Here, we generally observe larger discrepancies between the two measurements, but still, they fall

TABLE IV. Comparison of measurements from the XTCAV with our reconstruction for the smaller chirp case. The SASE bandwidth was estimated in the text as 4.1 eV. The uncertainties in the reconstructed values reflect a ±0.5 eV assumed uncertainty in the SASE bandwidth.

| Parameter | XTCAV | Spectral reconstruction |
|---|---|---|
| rms Duration (fs) | $9 \pm 2$ | $8.7 \pm 1.0$ |
| Chirp (MeV/μm) | $4.7 \pm 0.2$ | $4.7 \pm 0.5$ |
| Resolution (eV) | Not applicable | 0.35 |

TABLE V. Comparison of measurements from the XTCAV with our reconstruction for the larger chirp case. The SASE bandwidth was estimated in the text as 5 eV. The uncertainties in the reconstructed values reflect a ±0.5 eV assumed uncertainty in the SASE bandwidth.

| Parameter | XTCAV | Spectral reconstruction |
|---|---|---|
| rms duration (fs) | $6 \pm 3$ | $3.4 \pm 0.3$ |
| Chirp (MeV/μm) | $14.7 \pm 1.8$ | $16.3 \pm 1.4$ |
| Resolution (eV) | Not applicable | 0.48 |

within their errors of each other. The XTCAV measurements in this case are particularly sensitive to the few femtosecond temporal resolution since the few femtosecond x-ray pulse duration is near the resolution limit. The spectrometer resolution measured in this case was 0.48 eV which is again close to the expected value for this setup.

The discrepancy in the two spectrometer resolution measurements is not initially expected since the resolutions should not depend on the FEL working point. We point out the fact that the XFEL pulses are not exactly Gaussian and that the e-beam phase space has nonlinearities. However, both measured resolutions are close to the expected value, and the agreements with XTCAV measurements in the other parameters are quite good, proving the utility of the technique.

## V. DISCUSSION

The results of the previous section are promising and imply that our spectral reconstruction method can be a valuable tool in the accelerator control room. We would like to point out the use of the postsaturation taper in the experiment and what it means for our model's applicability. A postsaturation taper has been shown to preserve some of the coherence properties of the exponential gain regime which otherwise deteriorate after saturation [38]. Furthermore, the zero-chirp spectral reconstruction method was empirically shown to apply in the postsaturation taper regime [15]. This implies that the basic statistics we are trying to take advantage of still work with a taper. It also implies that the taper should not interfere with chirp-related statistics, or else the zero chirp approach would have had issues. In the future, we will study the effect of tapering on our method further, both in simulation and in experiments.

With that established, we will now consider future applications and improvements to the method. The model presented in Appendix B is initially very general, simply considering a radiation source that consists of a number of chirped emitters described by a known time-independent Green's function. It is only in Appendix C that we specialize to the case of the FEL. As such, in principle, the same formalism may be able to describe other radiation sources, such as radiation emitted by beams in bending magnets. This follows early work studying incoherent fluctuations in synchrotron radiation, which similarly showed that such incoherent fluctuations contained information about the electron bunch length [16,18]. With an application of our method to that area, one could in principle extract both bunch length and chirp at a bunch compressor, where the chirp is an essential component of the beam phase space.

A natural question would be the extent to which the model can be applied to nonlinear chirps. This would require an appropriate Green's function that can capture the effect of a nonlinear chirp. Our revision of the FEL Green's function derivation in Appendix A is already sufficiently general to perform that analysis. An in-depth analysis of spectral correlations in the presence of chirp nonlinearity will be the subject of a future publication.

We foresee our method as a useful tool to assist in accelerator control room operations, in particular, when an XTCAV is unavailable. Often users request specific spectrotemporal properties of the pulse, such as broad bandwidth for x-ray absorption spectroscopy or ultrashort pulses for atomic physics. The method presented here provides a useful spectral diagnostic to understand the properties of the x-ray pulse and can therefore assist in getting these operating modes set up efficiently and accurately. With a nondestructive spectrometer [32], our method can be used to set up a real-time diagnostic of average pulse length and chirp for these purposes.

## VI. CONCLUSIONS

We have presented an extension of the method of [15] that allows for proper accounting of linear energy chirp in the electron beam driving an XFEL. With our revised model, one can reconstruct the x-ray pulse length, electron beam chirp, and spectrometer resolution from a multishot measurement of the XFEL spectrum, as long as the spectrometer resolution is not much larger than the SASE spectral coherence. We have numerically shown our method to be robust to 3D effects as well as early saturation effects, thus ensuring its applicability in practical experimental settings. Furthermore, we have provided experimental results suggesting that the method may also be applicable with a postsaturation taper, but this subject requires further study. This approach should be especially useful for FEL facilities that lack an XTCAV system but can also be useful as a complementary measurement to the XTCAV. We hope to perform additional experiments to further understand the limitations and uses of the approach.

## ACKNOWLEDGMENTS

The authors thank Marion Harmand (UPMC) and the other authors of [35] for their permission to use the experimental data. We also thank William Fawley, Erik Hemsing, Agostino Marinelli, and Zhirong Huang (SLAC) for helpful discussions about FEL theory and simulations. Finally, we thank Diling Zhu (SLAC) for discussions of x-ray diagnostics. This work was supported by the

Department of Energy, Laboratory Directed Research and Development program at SLAC National Accelerator Laboratory, under Contract No. DE-AC02-76SF00515. R. R. R. acknowledges the support of the William R. Hewlett fellowship and the Robert H. Siemann fellowship.

## APPENDIX A: GREEN'S FUNCTION FOR THE 1D FEL WITH LINEAR CHIRP

We revise the derivation of the 1D FEL Green's function similar to the approach by Krinsky and Huang [26]. We will start with the FEL pendulum equations:

$$\frac{d\theta}{dZ} = p \qquad \frac{dp}{dZ} = -\frac{2D_2}{\gamma_0^2}(Ae^{i\theta} + A^* e^{-i\theta}), \quad \text{(A1)}$$

where $\theta = (k_0 + k_u)z - \omega_0 t$ is the ponderomotive phase with $\omega_0 = ck_0$, the resonant FEL frequency and $k_u$, the undulator wavenumber. Additionally, $p = 2(\gamma - \gamma_0)/\gamma_0$ is the relative energy detuning of the electron from the resonance energy $\gamma_0$. $D_2$ is a coupling factor defined in [26]. Finally, $Z = k_u z$ is the distance into the undulator measured in the phase of the magnetic field, and the FEL field is $E(\theta, Z) = A(\theta, Z)e^{i(\theta - Z)} + \text{c.c.}$ where $A(\theta, Z)$ is the slowly varying envelope of the x-ray field. The pendulum equations can be combined into a single Vlasov equation for the distribution function describing the electron beam phase space $\psi(\theta, p, Z)$:

$$\frac{\partial \psi}{\partial Z} + p\frac{\partial \psi}{\partial \theta} - \frac{2D_2}{\gamma_0^2}(Ae^{i\theta} + A^* e^{-i\theta})\frac{\partial \psi}{\partial p} = 0. \quad \text{(A2)}$$

This must be combined with a Maxwell equation for the field to fully describe the system

$$\left(\frac{\partial}{\partial Z} + \frac{\partial}{\partial \theta}\right)A = \frac{D_1}{\gamma_0} e^{-i\theta} \int \psi(\theta, p, Z) dp, \quad \text{(A3)}$$

where $D_1$ is another coupling factor defined in [26], and $2D_1 D_2 = (2\rho)^3 \gamma_0^3$ with $\rho$, the FEL Pierce parameter. The FEL process induces microbunching in the electron beam at the FEL frequency, which modifies the high-frequency spectral content of the beam distribution but leaves the macroscopic properties of the beam unchanged before saturation. As such, we decompose the distribution function into $\psi(\theta, p, Z) = \psi_0(\theta, p, Z) + \psi_1(\theta, p, Z)$. Here, $\psi_0$ represents the macroscopic beam distribution while $\psi_1$ represents any initial and FEL-induced microbunching. Under the assumption that the former is much larger than the latter, and further that the two quantities vary on disparate timescales, the Vlasov equation can be split into two linearized equations for the two components:

$$\frac{\partial \psi_0}{\partial Z} + p\frac{\partial \psi_0}{\partial \theta} = 0 \quad \text{(A4)}$$

$$\frac{\partial \psi_1}{\partial Z} + p\frac{\partial \psi_1}{\partial \theta} = \frac{2D_2}{\gamma_0^2} Ae^{i\theta}\frac{\partial \psi_0}{\partial p} \quad \text{(A5)}$$

We note that in writing these down, we also neglected the complex conjugate $A^* e^{-i\theta}$, as it has been shown in the past that this term is relevant only for few-cycle x-ray pulses [39] while here we are interested in pulses that are long relative to the FEL coherence length. The equation for the microbunching is made up of a homogeneous part which is identical to the equation for $\psi_0$ as well as an inhomogeneous part. If $\psi_0(\theta, p, 0) = \Psi_0(\theta, p)$, then the solution to the first equation is just $\Psi_0(\theta - pZ, p)$. Similarly, if $\psi_1(\theta, p, 0) = \Psi_1(\theta, p)$, then the first part of the solution for $\psi_1$ is $\Psi_1(\theta - pZ, p)$. The second part, which solves the inhomogeneous equation, can be obtained and yields the microbunching distribution in the form

$$\psi_1(\theta, p, Z) = \Psi_1(\theta - pZ, p) + \frac{2D_2}{\gamma_0^2} e^{i\theta}\frac{\partial \Psi_0}{\partial p}\bigg|_{(\theta - pZ, p)} \int_0^Z dZ' A(\theta - p(Z - Z'), Z')e^{-ip(Z - Z')}. \quad \text{(A6)}$$

This solution can be further simplified by assuming that both $\Psi_0$ and $A$ are slowly varying functions of the phase $\theta$. As such, for relatively small chirps, we may neglect the corrections to their phase arguments. If we further note that the initial distribution function is simply the sum of the initial values of the two parts, $\psi(\theta, p, 0) = \Psi_0(\theta, p) + \Psi_1(\theta, p)$, then we may finally write the solution for the full distribution function as

$$\psi(\theta, p, Z) = \psi(\theta - pZ, p, 0) + \frac{2D_2}{\gamma_0^2} e^{i\theta}\frac{\partial \Psi_0}{\partial p}\int_0^Z dZ' A(\theta, Z')e^{-ip(Z - Z')}. \quad \text{(A7)}$$

The initial particle distribution is considered in Klimontovich form as an explicit sum over electrons in the beam

$$\psi(\theta, p, 0) = \sum_j \delta(p - p_j)\delta(\theta - \theta_j), \quad \text{(A8)}$$

where here $p_j$ and $\theta_j$ are the initial values of $p$ and $\theta$ for the $j$th electron at the undulator entrance. We can now plug the distribution function solution equation (A7) into the Maxwell equation (A3), yielding

$$\left(\frac{\partial}{\partial Z}+\frac{\partial}{\partial\theta}\right)A=\frac{D_1}{\gamma_0}\sum_j e^{-i\theta}\delta(\theta-\theta_j-p_jZ)+i(2\rho)^3\int_0^Z dZ'A(\theta,Z')(Z-Z')\int dp\Psi_0(\theta,p)e^{-ip(Z-Z')}, \tag{A9}$$

where we have integrated the last term by parts with respect to $p$. Now following Krinsky and Huang, we will replace $e^{-i\theta}$ with $e^{-i\theta_j-ip_jZ}$ and subsequently neglect $p_jZ$ relative to $\theta-\theta_j$ in the delta function, which is equivalent to assuming that any energy spread is too small to change the current profile through the undulator. We solve Eq. (A9) by introducing the Laplace transform of the field $\hat{A}(\theta,s)=\int_0^\infty dZA(\theta,Z)e^{-sZ}$:

$$s\hat{A}+\frac{\partial\hat{A}}{\partial\theta}=\frac{D_1}{\gamma_0}\sum_j\frac{e^{-i\theta_j}}{s+ip_j}\delta(\theta-\theta_j)+i(2\rho)^3\hat{A}\int dp\frac{\Psi_0(\theta,p)}{(s+ip)^2}, \tag{A10}$$

where we have assumed that the initial x-ray field is zero so that we can focus on SASE radiation. This is solved by moving the final term over to the left-hand side and writing the left-hand side as a single derivative with respect to $\theta$, with the result

$$\hat{A}(\theta,s)=\frac{D_1}{\gamma_0}\sum_j\frac{e^{-i\theta_j}}{s+ip_j}\exp\left[-s(\theta-\theta_j)+i(2\rho)^3\int_{\theta_j}^{\theta}d\theta'\int dp\frac{\Psi_0(\theta',p)}{(s+ip)^2}\right] \tag{A11}$$

and by inverse Laplace transforming, we find the slowly varying envelope of the SASE field

$$A(\theta,Z)=\frac{D_1}{\gamma_0}\sum_j\int\frac{ds}{2\pi i}\frac{e^{-i\theta_j}}{s+ip_j}\exp\left[sZ-s(\theta-\theta_j)+i(2\rho)^3\int_{\theta_j}^{\theta}d\theta'\int dp\frac{\Psi_0(\theta',p)}{(s+ip)^2}\right] \tag{A12}$$

This result is quite general. We will now specialize to the case in question. In particular, we consider a separable distribution function $\Psi_0(\theta,p)=f(\theta)V(p+\mu\theta)$, where $f(\theta)$ is the current profile of the electron beam and $V(p)$ is the uncorrelated energy distribution which has been chirped by $-\mu\theta$. If we further simplify to zero uncorrelated energy spread, then $V(p)=\delta(p)$ and we can write the SASE field as

$$A(\theta,Z)=\frac{D_1}{\gamma_0}\sum_j\int\frac{ds}{2\pi i}\frac{e^{-i\theta_j}}{s-i\mu\theta_j}\exp\left[sZ-s(\theta-\theta_j)+i(2\rho)^3\int_{\theta_j}^{\theta}d\theta'\frac{f(\theta')}{(s-i\mu\theta')^2}\right] \tag{A13}$$

The final integral can be dealt with if we assume the bunch to be long relative to a coherence length, as in this case, we may approximate $f(\theta')$ by $f(\theta_j)$ and pull it out of the integral. This results in

$$A(\theta,Z)=\frac{D_1}{\gamma_0}\sum_j\int\frac{ds}{2\pi i}\frac{e^{-i\theta_j}}{s-i\mu\theta_j}\exp\left[sZ-s(\theta-\theta_j)+i(2\rho f(\theta_j)^{1/3})^3\frac{\theta-\theta_j}{(s-i\mu\theta)(s-i\mu\theta_j)}\right], \tag{A14}$$

where we have pulled the $f(\theta_j)$ into the cube in order to stress that the FEL with long bunch time-dependent effects acts just like the time-independent FEL with a time-dependent Pierce parameter $\rho_{\rm td}(\theta_j)=\rho f(\theta_j)^{1/3}$. The final step to get to the Green's function is to shift our Laplace variable from $s$ to $s-i\mu\theta_j$, in which case we have finally

$$A(\theta,Z)=\frac{D_1}{\gamma_0}\sum_j e^{-i\theta_j}e^{-i\mu\theta_j(\theta-Z-\theta_j)}\left(\int\frac{ds}{2\pi is}\exp\left[sZ-s(\theta-\theta_j)+i[2\rho_{\rm td}(\theta_j)]^3\frac{\theta-\theta_j}{s[s-i\mu(\theta-\theta_j)]}\right]\right) \tag{A15}$$

What we have enclosed in parentheses is our full Green's function including time-dependent effects. It is identical to that derived by Krinsky and Huang [Eqs. (A12) and (A13) of [26]] except for the time-dependent value of $\rho$, which was omitted in Ref. [26] due to an infinitely long electron beam assumption. Of course, this is still not quite in the expected final form. We will now evaluate the contour integral with a saddle point approximation, whereby we estimate an integral of the form $\int dsP(s)e^{F(s)}\simeq P(s_0)e^{F(s_0)}\sqrt{-2\pi/F''(s_0)}$ where $F'(s_0)=0$ and $F(s_0)\gg 1$. For our case, the condition $F'(s_0)=0$ yields a cubic equation that will have one root with a positive real part. Only this root is of interest to us, since when plugged into $e^{s_0Z}$, it gives rise to an exponential gain of the radiation field. We solve for this root to second order in $\mu$, yielding

$$s_0\simeq\frac{2^{4/3}i^{1/3}(\theta-\theta_j)^{1/3}\rho_{\rm td}(\theta_j)}{(Z-\theta+\theta_j)^{1/3}}+\frac{i\mu}{2}(\theta-\theta_j)+\frac{i^{5/3}(Z-\theta+\theta_j)^{1/3}(\theta-\theta_j)^{5/3}}{12\times 2^{1/3}\rho_{\rm td}(\theta_j)}\mu^2 \tag{A16}$$

This is still much more complicated than the terms in the Green's function reported by Krinsky and Huang. This is because they apply one more approximation, which is to expand the resulting Green's function around $\theta - \theta_j = Z/3$ where $s_0'(\theta - \theta_j) \simeq 0$. Note that this corresponds to expanding around the value of $\theta$ given by the SASE group velocity. The result is

$$g(\theta,\theta_j,Z) \propto \exp\left[\rho_{\rm td}(\theta_j)(\sqrt{3}+i)Z - \frac{9\rho_{\rm td}(\theta_j)}{4Z}(\sqrt{3}+i)\left(\theta-\theta_j-\frac{Z}{3}\right)^2 + \frac{i\mu}{2}(\theta-\theta_j)(Z-\theta+\theta_j)\right]$$
$$\times \exp\left[+\frac{Z^3\mu^2}{288\rho_{\rm td}(\theta_j)}(-\sqrt{3}+i) - \frac{Z\mu^2}{96\rho_{\rm td}(\theta_j)}(-\sqrt{3}+i)\left(\theta-\theta_j-\frac{2Z}{3}\right)^2 + \mathcal{O}(\mu^3)\right] \tag{A17}$$

Equation (A17) is a generalized form of Krinsky and Huangs' result which accounts for both a finite bunch length and higher-order chirp effects. We can delineate a few distinct parts of the Green's function. First is a purely time-dependent part we will call $h_{\rm td}(\theta_j)$ which contains the first and fourth terms of Eq. (A17). We call it time-dependent because it is explicitly a function of the arrival time of electron $j$ at the undulator, as opposed to the relative time $\theta - \theta_j$. Notice that this captures not only time-dependent gain effects of a nonconstant current profile in the form of $\rho_{\rm td}(\theta_j)$ but also gain reduction due to the chirp which is of order $\mu^2$. This gain reduction was mentioned but not written out in [26]. There is also, of course, higher-order time-dependent gain reduction, however, it is all implicitly captured by $h_{\rm td}$.

The second part of the Green's function is made up of the second and third terms in Eq. (A17). We will discuss the fifth term below. The second and third terms are almost only a function of the relative phase $\theta - \theta_j$. We say almost because the first and last terms still depends on $\rho_{\rm td}(\theta_j)$. This amounts to the time dependence of the SASE bandwidth of the pulse. We propose to replace this with $\rho$ as was done without explicit mention in [15]. This choice seems to work empirically or else the original method proposed in [15] would not have worked. We can justify the choice in two ways: first, since we know empirically that the statistics of the radiation are not highly sensitive to the value of the SASE bandwidth, it should not make a large difference to approximate the bandwidth in this way. Second, most of the radiation will be emitted where the current profile peaks, which is generally where $\rho_{\rm td}(\theta_j)$ varies the slowest. Finally, we note that this is not a problem for long flattopped beams, for which slippage is unimportant and $\rho_{\rm td}$ is constant within the beam current.

The third term is purely time independent without ambiguity, and it accounts for the local chirp of the coherent SASE spikes [26]. There are similarly higher-order, largely time-independent terms that we have neglected such as the fifth, but we have found that the effect of the linear order term even on relatively large chirps is weak. In particular, neglecting the third term is equivalent to approximating $\delta_u$ as $u\sigma_t/\sigma_\omega$ in Eqs. (7) and (8). As we argued then, that is a good approximation for sufficiently long pulses. Since even the linear order term has a small effect on reconstructions, these second and higher-order time-independent terms can almost always be neglected. Further studies taking them into account could be the subject of future work.

With this definition of $h_{\rm td}$ as well as the replacement of $\rho_{\rm td}$ with $\rho$ in the second term of Eq. (A17), we arrive finally at the form of the Green's function used in the paper, Eqs. (4) and (5), once written in terms of time rather than phase. We did not deal explicitly with the effect of taper in our analysis, but the same logic applies in showing that its effects on the gain can be subsumed into $h_{\rm td}$, as was found empirically in [15]. We expect this to be true at least for a postsaturation taper, which is in general small and unrelated to the beam chirp. More tailored tapers, such as chirp-taper matching, would require more careful analysis.

## APPENDIX B: DERIVATION OF $G_2$ FORMULAS FOR RADIATION FROM DISCRETE CHIRPED EMITTERS

With the definitions of $G_2$ and $\tilde{S}(\omega)$ as in Eqs. (2) and (3), it was shown in [15] that $G_2$ can be written as

$$G_2(\delta\omega) = \frac{\int d\Delta d\Omega e^{-\frac{\Delta^2}{4\sigma_m^2}-\frac{\Omega^2}{\sigma_m^2}}\langle|\tilde{E}(\omega+\Omega+(\Delta+\delta\omega)/2|^2|\tilde{E}(\omega+\Omega-(\Delta+\delta\omega)/2)|^2\rangle}{\int d\Delta d\Omega e^{-\frac{\Delta^2}{4\sigma_m^2}-\frac{\Omega^2}{\sigma_m^2}}\langle|\tilde{E}(\omega+\Omega+(\Delta+\delta\omega)/2|^2\rangle\langle|\tilde{E}(\omega+\Omega-(\Delta+\delta\omega)/2)|^2\rangle} - 1 \tag{B1}$$

Thus, we see that it will be useful to calculate the spectral field correlation $\langle\tilde{E}(\omega-\delta\omega/2)\tilde{E}^*(\omega+\delta\omega/2)\rangle$ as well as the spectral intensity correlation $\langle|\tilde{E}(\omega-\delta\omega/2)|^2|\tilde{E}(\omega+\delta\omega/2|^2\rangle$. With the definition of the spectral field from Eq. (6), it follows that the spectral field correlation function is

$$\left\langle \tilde{E}\left(\omega-\frac{\delta\omega}{2}\right)\tilde{E}^*\left(\omega+\frac{\delta\omega}{2}\right)\right\rangle = \left\langle \sum_{j,k} e^{i\frac{z}{c}(\omega_j-\omega_k)} e^{i(\omega-\frac{\delta\omega}{2})t_j} e^{-i(\omega+\frac{\delta\omega}{2})t_k} \tilde{g}\left(\omega-\frac{\delta\omega}{2}-\omega_j\right)\tilde{g}^*\left(\omega+\frac{\delta\omega}{2}-\omega_k\right) h_{\mathrm{td}}(t_j)h^*_{\mathrm{td}}(t_k)\right\rangle \tag{B2}$$

Following Ref. [40] and considering only the incoherent portion of the sum, we restrict our attention to the terms where $j=k$, leaving

$$\left\langle \tilde{E}\left(\omega-\frac{\delta\omega}{2}\right)\tilde{E}^*\left(\omega+\frac{\delta\omega}{2}\right)\right\rangle = \left\langle \sum_{j} e^{-i\delta\omega t_j} \tilde{g}\left(\omega-\frac{\delta\omega}{2}-\omega_j\right)\tilde{g}^*\left(\omega+\frac{\delta\omega}{2}-\omega_j\right)|h_{\mathrm{td}}(t_j)|^2\right\rangle \tag{B3}$$

Let us move on now to the spectral intensity correlation, which is

$$\begin{aligned}\left\langle \left|\tilde{E}\left(\omega-\frac{\delta\omega}{2}\right)\right|^2\left|\tilde{E}\left(\omega+\frac{\delta\omega}{2}\right)\right|^2\right\rangle = \Bigg\langle \sum_{k,j,l,m} & e^{i\frac{z}{c}(\omega_k-\omega_j+\omega_l-\omega_m)} e^{i\omega(t_k-t_j+t_l-t_m)-i\frac{\delta\omega}{2}(t_k-t_j-t_l+t_m)} \\ & \tilde{g}\left(\omega-\frac{\delta\omega}{2}-\omega_k\right)\tilde{g}^*\left(\omega-\frac{\delta\omega}{2}-\omega_j\right)\tilde{g}\left(\omega+\frac{\delta\omega}{2}-\omega_l\right)\tilde{g}^*\left(\omega+\frac{\delta\omega}{2}-\omega_m\right) h_{\mathrm{td}}(t_k)h^*_{\mathrm{td}}(t_j)h_{\mathrm{td}}(t_l)h^*_{\mathrm{td}}(t_m)\Bigg\rangle\end{aligned} \tag{B4}$$

Now again following [40], we will consider only two sets of terms in these sums: $k=j$, $l=m$, $k\neq l$; and $k=m$, $l=j$, $k\neq l$. This leaves us with

$$\begin{aligned}\left\langle \left|E\left(\omega-\frac{\delta\omega}{2}\right)\right|^2\left|E\left(\omega+\frac{\delta\omega}{2}\right)\right|^2\right\rangle = & \left\langle \sum_k |h_{\mathrm{td}}(t_k)|^2\left|\tilde{g}\left(\omega-\frac{\delta\omega}{2}-\omega_k\right)\right|^2\right\rangle\left\langle \sum_l |h_{\mathrm{td}}(t_l)|^2\left|\tilde{g}\left(\omega+\frac{\delta\omega}{2}-\omega_l\right)\right|^2\right\rangle \\ & + \left\langle \sum_k e^{-i\delta\omega t_k}|h_{\mathrm{td}}(t_k)|^2\tilde{g}\left(\omega-\frac{\delta\omega}{2}-\omega_k\right)\tilde{g}^*\left(\omega+\frac{\delta\omega}{2}-\omega_k\right)\right\rangle \\ & \times \left\langle \sum_l e^{-i\delta\omega t_l}|h_{\mathrm{td}}(t_l)|^2\tilde{g}\left(\omega-\frac{\delta\omega}{2}-\omega_l\right)\tilde{g}^*\left(\omega+\frac{\delta\omega}{2}-\omega_l\right)\right\rangle^*\end{aligned} \tag{B5}$$

Note that we can write the results we have found thus far more succinctly by defining

$$F(\omega,\delta\omega) \equiv \left\langle \sum_k e^{-i\delta\omega t_k}|h_{\mathrm{td}}(t_k)|^2\tilde{g}\left(\omega-\frac{\delta\omega}{2}-\omega_k\right)\tilde{g}^*\left(\omega+\frac{\delta\omega}{2}-\omega_k\right)\right\rangle \tag{B6}$$

With this function, we can write simply that

$$\left\langle E\left(\omega-\frac{\delta\omega}{2}\right)E^*\left(\omega+\frac{\delta\omega}{2}\right)\right\rangle = F(\omega,\delta\omega) \tag{B7}$$

$$\left\langle \left|E\left(\omega-\frac{\delta\omega}{2}\right)\right|^2\left|E\left(\omega+\frac{\delta\omega}{2}\right)\right|^2\right\rangle = F\left(\omega-\frac{\delta\omega}{2},0\right)F\left(\omega+\frac{\delta\omega}{2},0\right)+|F(\omega,\delta\omega)|^2 \tag{B8}$$

Notice then that $F(\omega,0)$ is proportional to the spectral intensity at frequency $\omega$. Furthermore, $G_2$ can be written as

$$G_2(\delta\omega) = \frac{\int d\Delta d\Omega e^{-\frac{\Delta^2}{4\sigma_m^2}-\frac{\Omega^2}{\sigma_m^2}}|F(\omega+\Omega,\Delta+\delta\omega)|^2}{\int d\Delta d\Omega e^{-\frac{\Delta^2}{4\sigma_m^2}-\frac{\Omega^2}{\sigma_m^2}}F(\omega+\Omega+\frac{\Delta+\delta\omega}{2},0)F(\omega+\Omega-\frac{\Delta+\delta\omega}{2},0)}. \tag{B9}$$

For ease of calculation, we note that we may replace the average of the sum over electrons with an integral over the average electron current profile $f(t)$ as

$$F(\omega,\delta\omega) = \int dt_j f(t_j)|h_{\mathrm{td}}(t_j)|^2 e^{-i\delta\omega t_j}\tilde{g}\left(\omega-\frac{\delta\omega}{2}-\omega_j\right)\tilde{g}^*\left(\omega+\frac{\delta\omega}{2}-\omega_j\right) \tag{B10}$$

So far we have left $h_{\mathrm{td}}(t_j)$ unspecified, which makes this equation difficult to evaluate. We may connect it to the average x-ray intensity profile $\chi(t)$ by noting

$$\chi(t) \equiv \langle |E(t)|^2 \rangle = \int dt_j f(t_j) |h_{\mathrm{td}}(t_j)|^2 |g(t - t_j)|^2 \tag{B11}$$

This is an integral of a product of terms with distinct timescales. The characteristic timescale of $g(t)$ is the inverse of the SASE bandwidth $1/\sigma_\omega$, whereas the timescale of $f(t)|h_{\mathrm{td}}(t)|^2$ is the electron bunch length. If the driving electron bunch has features that are long relative to the inverse of the SASE bandwidth, then the gain function $g(t)$ acts like a delta function when convolved with $f(t_j)|h_{\mathrm{td}}(t_j)|^2$. In other words, if $\sigma_t \sigma_\omega \gg 1$, we may write $\chi(t) \propto f(t)|h_{\mathrm{td}}(t)|^2$. As justification for this approximation, we note that typical SASE bandwidths for hard x rays are on the order of a few eV, whereas electron bunches are typically a few to tens of femtoseconds long. The product $\sigma_t \sigma_\omega$ is thus of order 10–100 for typical operating conditions. Another way of putting this is that the pulse is made up of many independent SASE spikes. Then up to a multiplicative factor which drops out of $G_2$, we can write

$$F(\omega, \delta\omega) = \int dt_j \chi(t_j) e^{-i\delta\omega t_j} \tilde{g}\left(\omega - \frac{\delta\omega}{2} - \omega_j\right) \tilde{g}^*\left(\omega + \frac{\delta\omega}{2} - \omega_j\right). \tag{B12}$$

Since up to this point, we have made no assumptions as to the particular form of the Green's function or the electron bunch except that we are focused on the incoherent part of the spectrum, these formulas can be applied to any radiation process describable by a Green's function.

## APPENDIX C: EVALUATION OF $G_2$ FORMULAS FOR FREE-ELECTRON LASER RADIATION

For a FEL driven by a chirped electron beam, $\tilde{g}(\omega)$ is the Fourier transform of Eq. (5) and $F$ can be evaluated with Eq. (B12). This results in the integral form

$$\begin{aligned} F(\omega, \delta\omega) = \int dt \chi(t) \exp\left[\frac{1}{1 + \hat{u} + \hat{u}^2}\left(-i\delta\omega t\left(1 + \frac{\hat{u}}{2}\right) - \frac{\delta\omega^2}{8\sigma_\omega^2} - \frac{u^2}{2\sigma_\omega^2}\left(t - \frac{z}{2\delta v} - \frac{\omega - \omega_0}{u}\right)^2\right)\right] \\ \times \exp\left\{-\frac{i\delta\omega}{24\sigma_\omega^2(1 + \hat{u} + \hat{u}^2)}[6\sigma_\omega^2(\hat{u}(1 + 2\hat{u})(z_0 + z_c) + 2(2 + \hat{u})z_g) + 4\sqrt{3}(1 + 2\hat{u})(\omega - \omega_0)]\right\} \end{aligned} \tag{C1}$$

where we have defined

$$\frac{1}{\delta v} = \frac{1}{c} + \frac{1}{v_0} - \frac{2}{v_g} \tag{C2}$$

and $\hat{u} = u/\sqrt{3}\sigma_\omega^2$. We note here that for the two cases of interest to us, namely $|F(\omega, \delta\omega)|$ and $F(\omega, 0)$, the second line vanishes and we are left with just the first. There is not much more that can be done with this integral analytically without specifying the pulse shape $\chi(t)$. This expression can be integrated for a Gaussian pulse $\chi(t) = e^{-t^2/2\sigma_t^2}$, for example, and yields the expressions given in Eqs. (7) and (9). Beyond explicit evaluation for particular pulse profiles, to elucidate the meaning of the equations, we have derived so far it is interesting to take limit that the pulse contains many SASE spikes, or $\sigma_t \sigma_\omega \gg 1$ where $\sigma_t$ is a measure of the length of the x-ray pulse. In this limit, the exponential factor varies much more quickly than the pulse profile, and we may replace $\chi(t)$ in the integrand by $\chi(\frac{z}{2\delta v} + \frac{\omega - \omega_0}{u})$. In this case, the integral can be taken explicitly, leaving us with

$$F(\omega, \delta\omega) \propto \chi\left(\frac{z}{2\delta v} + \frac{\omega - \omega_0}{u}\right) \exp\left[-\frac{\delta\omega^2}{2}\left(\frac{1}{4\sigma_\omega^2} + \frac{\sigma_\omega^2}{u^2}\left(\frac{1 + \frac{\hat{u}}{2}}{1 + \hat{u} + \hat{u}^2}\right)^2\right) - i\delta\omega\left(\frac{z}{2\delta v} + \frac{\omega - \omega_0}{u}\right)\frac{1 + \frac{\hat{u}}{2}}{1 + \hat{u} + \hat{u}^2}\right]. \tag{C3}$$

In this limit, then the spectrum of the radiation is given by

$$F(\omega, 0) \propto \chi\left(\frac{z}{2\delta v} + \frac{\omega - \omega_0}{u}\right) \tag{C4}$$

In other words, when the chirp dominates over the SASE bandwidth, the spectrum is a direct mapping of the temporal profile of the pulse. Meanwhile, $G_2$ can be calculated as (neglecting spectrometer resolution)

$$G_2(\delta\omega) = \exp\left[-\delta\omega^2\left(\frac{1}{4\sigma_\omega^2} + \frac{\sigma_\omega^2}{u^2}\left(\frac{1+\frac{\hat{u}}{2}}{1+\hat{u}+\hat{u}^2}\right)^2\right)\right] \quad \text{(C5)}$$

and to lowest order in $\hat{u}$

$$G_2(\delta\omega) = \exp\left[-\frac{\delta\omega^2\sigma_\omega^2}{u^2}\right]. \quad \text{(C6)}$$

Referring back to [26], $\sigma_\omega/u$ is precisely the length of a single frequency slice of linearly chirped radiation. In other words, as the bunch gets longer and longer for a fixed chirp, the statistics become dominated by the chirp rather than the SASE process and an estimate of pulse length based solely on $G_2$ will saturate at the value $\sigma_\omega/u$, precisely as we see in Fig. 3.


[1] R. Bonifacio, C. Pellegrini, and L. Narducci, Collective instabilities and high-gain regime free electron laser, AIP Conf. Proc. **118**, 236 (1984).

[2] C. Pellegrini, Progress toward a soft x-ray FEL, Nucl. Instrum. Methods Phys. Res., Sect. A **272**, 364 (1988).

[3] Y. S. Derbenev, A. Kondratenko, and E. Saldin, On the possibility of using a free electron laser for polarization of electrons in storage rings, Nucl. Instrum. Methods Phys. Res. **193**, 415 (1982).

[4] P. Emma, R. Akre, J. Arthur, R. Bionta, C. Bostedt, J. Bozek, A. Brachmann, P. Bucksbaum, R. Coffee, F.-J. Decker *et al.*, First lasing and operation of an ångstrom-wavelength free-electron laser, Nat. Photonics **4**, 641 (2010).

[5] C. Pellegrini, X-ray free-electron lasers: From dreams to reality, Phys. Scr. **2016**, 014004 (2017).

[6] Y. Ding, C. Behrens, P. Emma, J. Frisch, Z. Huang, H. Loos, P. Krejcik, and M. Wang, Femtosecond x-ray pulse temporal characterization in free-electron lasers using a transverse deflector, Phys. Rev. ST Accel. Beams **14**, 120701 (2011).

[7] C. Behrens, F.-J. Decker, Y. Ding, V. Dolgashev, J. Frisch, Z. Huang, P. Krejcik, H. Loos, A. Lutman, T. Maxwell *et al.*, Few-femtosecond time-resolved measurements of x-ray free-electron lasers, Nat. Commun. **5**, 3762 (2014).

[8] M. Altarelli, R. Brinkmann, and M. Chergui, The European X-ray Free-Electron Laser, Technical design report, DESY, Technical Report No. 06-097, 2007.

[9] G. Geloni, V. Kocharyan, and E. Saldin, Ultrafast x-ray pulse measurement method, arXiv:1001.3544.

[10] Y. Ding, F.-J. Decker, P. Emma, C. Feng, C. Field, J. Frisch, Z. Huang, J. Krzywinski, H. Loos, J. Welch *et al.*, Femtosecond X-Ray Pulse Characterization in Free-Electron Lasers Using a Cross-Correlation Technique, Phys. Rev. Lett. **109**, 254802 (2012).

[11] S. Serkez, G. Geloni, M. Guetg, V. Kocharyan, S. Liu, and E. Saldin, Delay-detune scan for longitudinal electron beam characterization at free-electron lasers, Phys. Rev. Accel. Beams **23**, 122801 (2020).

[12] H. Li, Y. Sun, J. Vila-Comamala, T. Sato, S. Song, P. Sun, M. H. Seaberg, N. Wang, J. Hastings, M. Dunne *et al.*, Generation of highly mutually coherent hard-x-ray pulse pairs with an amplitude-splitting delay line, Phys. Rev. Res. **3**, 043050 (2021).

[13] T. Osaka, T. Hirano, Y. Morioka, Y. Sano, Y. Inubushi, T. Togashi, I. Inoue, K. Tono, A. Robert, K. Yamauchi *et al.*, Characterization of temporal coherence of hard x-ray free-electron laser pulses with single-shot interferograms, IUCrJ **4**, 728 (2017).

[14] Y. Inubushi, K. Tono, T. Togashi, T. Sato, T. Hatsui, T. Kameshima, K. Togawa, T. Hara, T. Tanaka, H. Tanaka *et al.*, Determination of the Pulse Duration of an X-Ray Free Electron Laser Using Highly Resolved Single-Shot Spectra, Phys. Rev. Lett. **109**, 144801 (2012).

[15] A. Lutman, Y. Ding, Y. Feng, Z. Huang, M. Messerschmidt, J. Wu, and J. Krzywinski, Femtosecond x-ray free electron laser pulse duration measurement from spectral correlation function, Phys. Rev. ST Accel. Beams **15**, 030705 (2012).

[16] M. Zolotorev and G. Stupakov, Spectral fluctuations of incoherent radiation and measurement of longitudinal bunch profile, in *Proceedings of the Particle Accelerator Conference, Vancouver, BC, Canada, 1997* (IEEE, New York, 1997), Vol. 2, pp. 2180–2182.

[17] J. Krzywinski, E. Saldin, E. Schneidmiller, and M. Yurkov, A new method for ultrashort electron pulse-shape measurement using synchrotron radiation from a bending magnet, Nucl. Instrum. Methods Phys. Res., Sect. A **401**, 429 (1997).

[18] F. Sannibale, G. Stupakov, M. Zolotorev, D. Filippetto, and L. Jägerhofer, Absolute bunch length measurements by incoherent radiation fluctuation analysis, Phys. Rev. ST Accel. Beams **12**, 032801 (2009).

[19] I. Lobach, S. Nagaitsev, V. Lebedev, A. Romanov, G. Stancari, A. Valishev, A. Halavanau, Z. Huang, and K.-J. Kim, Transverse Beam Emittance Measurement by Undulator Radiation Power Noise, Phys. Rev. Lett. **126**, 134802 (2021).

[20] S. Serkez, O. Gorobtsov, D. E. Rivas, M. Meyer, B. Sobko, N. Gerasimova, N. Kujala, and G. Geloni, Wigner distribution of self-amplified spontaneous emission free-electron laser pulses and extracting its autocorrelation, J. Synchrotron Radiat. **28**, 3 (2021).

[21] C. B. Schroeder, C. Pellegrini, S. Reiche, J. Arthur, and P. Emma, Chirped-beam two-stage free-electron laser for high-power femtosecond x-ray pulse generation, J. Opt. Soc. Am. B **19**, 1782 (2002).

[22] E. L. Saldin, E. A. Schneidmiller, and M. V. Yurkov, Self-amplified spontaneous emission FEL with energy-chirped electron beam and its application for generation of attosecond x-ray pulses, Phys. Rev. ST Accel. Beams **9**, 050702 (2006).

[23] H. Li, J. MacArthur, S. Littleton, M. Dunne, Z. Huang, and D. Zhu, Femtosecond-Terawatt Hard X-Ray Pulse Generation with Chirped Pulse Amplification on a Free Electron Laser, Phys. Rev. Lett. **129**, 213901 (2022).

[24] D. Gauthier, E. Allaria, M. Coreno, I. Cudin, H. Dacasa, M. B. Danailov, A. Demidovich, S. Di Mitri, B. Diviacco, E. Ferrari *et al.*, Chirped pulse amplification in an extreme-ultraviolet free-electron laser, Nat. Commun. **7**, 13688 (2016).

[25] A. A. Lutman, T. J. Maxwell, J. P. MacArthur, M. W. Guetg, N. Berrah, R. N. Coffee, Y. Ding, Z. Huang, A. Marinelli, S. Moeller *et al.*, Fresh-slice multicolour x-ray free-electron lasers, Nat. Photonics **10**, 745 (2016).

[26] S. Krinsky and Z. Huang, Frequency chirped self-amplified spontaneous-emission free-electron lasers, Phys. Rev. ST Accel. Beams **6**, 050702 (2003).

[27] M. Xie, Design optimization for an x-ray free electron laser driven by SLAC linac, in *Proceedings of the Particle Accelerator Conference, Dallas, TX, 1995* (IEEE, New York, 1995), Vol. 1, pp. 183–185.

[28] K.-J. Kim, Z. Huang, and R. Lindberg, *Synchrotron Radiation and Free-Electron Lasers* (Cambridge University Press, Cambridge, England, 2017).

[29] R. Robles, A. Halavanau, A. Lutman, D. Cesar, and G. Stupakov, Spectrometer-based x-ray free-electron laser pulse duration measurements of chirped beams, in *Proceedings of the 40th Free Electron Laser Conference (FEL'22), Trieste, Italy, 2022* (JACOW, Geneva, Switzerland, 2022).

[30] S. Reiche, Genesis 1.3: A fully 3D time-dependent FEL simulation code, Nucl. Instrum. Methods Phys. Res., Sect. A **429**, 243 (1999).

[31] G. L. Dakovski, P. Heimann, M. Holmes, O. Krupin, M. P. Minitti, A. Mitra, S. Moeller, M. Rowen, W. F. Schlotter, and J. J. Turner, The soft x-ray research instrument at the linac coherent light source, J. Synchrotron Radiat. **22**, 498 (2015).

[32] D. Zhu, M. Cammarata, J. M. Feldkamp, D. M. Fritz, J. B. Hastings, S. Lee, H. T. Lemke, A. Robert, J. L. Turner, and Y. Feng, A single-shot transmissive spectrometer for hard x-ray free electron lasers, Appl. Phys. Lett. **101**, 034103 (2012).

[33] S. Reiche, Genesis-1.3-version4, https://github.com/svenreiche/Genesis-1.3-Version4 (2022).

[34] A. Lutman, Z. Huang, J. Krzywinski, J. Wu, D. Zhu, and Y. Feng, Statistical characterization of an x-ray FEL in the spectral domain, in *Proceedings of Advances in X-ray Free-Electron Lasers Instrumentation IV*, SPIE Proceedings Vol. 10237 (SPIE-International Society for Optical Engineering, Bellingham, WA, 2017), pp. 51–60.

[35] M. Harmand, M. Cammarata, M. Chollet, A. Krygier, H. Lemke, and D. Zhu, Single-shot x-ray absorption spectroscopy at x-ray free electron lasers, arXiv:2005.01572.

[36] H. Loos, T. Borden, P. Emma, J. Frisch, and J. Wu, Relative bunch length monitor for the linac coherent light source (LCLS) using coherent edge radiation, in *Proceedings of the 22nd Particle Accelerator Conference, PAC-2007, Albuquerque, NM* (IEEE, New York, 2007), pp. 4189–4191.

[37] H. Loos, LCLS accelerator operation and measurement of electron beam parameters relevant for the x-ray beam, in *Proceedings of Advances in X-ray Free-Electron Lasers II: Instrumentation*, SPIE Proceedings Vol. 8778 (SPIE-International Society for Optical Engineering, Bellingham, WA, 2013), pp. 58–66.

[38] E. A. Schneidmiller and M. Yurkov, Statistical properties of the radiation from SASE FEL operating in a post-saturation regime with and without undulator tapering, J. Mod. Opt. **63**, 288 (2016).

[39] S. Krinsky, Transient analysis of free-electron lasers with discrete radiators, Phys. Rev. E **59**, 1171 (1999).

[40] E. L. Saldin, E. A. Schneidmiller, and M. Yurkov, Statistical properties of radiation from VUV and x-ray free electron laser, Opt. Commun. **148**, 383 (1998).